Large-area phosphorene for stable carbon-based perovskite solar cells

Check for updates

Purevlkham Myagmarsereejid[1], Selengesuren Suragtkhuu[1], Quang Thang Trinh [1], Tim Gould [1], Nam-Trung Nguyen [1], Munkhjargal Bat-Erdene[1,2], Eric Campbell[1], Minh Tam Hoang[3,4], Wei-Hsun Chiu [3,4], Qin Li[5], Hongxia Wang[3,4], Yu Lin Zhong [1] ✉ & Munkhbayar Batmunkh [1] ✉

Carbon-based perovskite solar cells (c-PSCs) have attracted increasing attention due to their numerous advantages including ease of fabrication, the potential of assembling flexible devices, low manufacturing costs as well as large-scale production. However, c-PSCs suffer from the limited hole extraction and high charge carrier recombination due to the inadequate interface contact between the carbon electrode and perovskite film. Herein, we report the fabrication of planar c-PSCs with high efficiency and excellent stability by employing electrochemically produced large-area phosphorene flakes as a hole-transporting layer (HTL). Large-area phosphorene shows well-aligned band energy levels with the perovskite, and thus led to the efficient hole extraction and the reduced hysteresis behaviour. Consequently, while exhibiting excellent stability under various harsh testing conditions, the devices with phosphorene HTL delivered a power conversion efficiency of over 15% with an open-circuit voltage of 1.082 V, which is the highest reported value for c-PSCs without traditional hole transporting materials to date.

Perovskite solar cells (PSCs) have shown remarkable advancement in the past two decades with rapid increases in their power conversion efficiency (PCEs) from 3.8% in 2009 to more than 26% today[1]. A typical high efficiency PSC is fabricated using a n-i-p device architecture with a layered structure of transparent conductive electrode, electron transporting layer (ETL), perovskite absorber, hole transporting layer (HTL) and metal electrode[2]. Although PSCs can achieve high efficiency upon fabrication, the challenges associated with their stability and use of expensive organic hole transporting materials (HTM) (e.g., 2,2',7,7'-Tetrakis[N,N-di(4-methoxyphenyl) amino]-9,9'-spirobifluorene (Spiro-OMETAD) and noble metal electrode (Au) limit the widespread commercialization of this cutting-edge technology[3–6]. To overcome these issues, carbon-based PSCs (c-PSCs) have been developed as they promise to be highly stable, low cost and scalable, while delivering good device performances[7,8]. To date, the highest reported power conversion efficiency (PCE) for HTM-free c-PSCs is 19.5% with a short-circuit current density (J_{SC}) of 23.50 mA cm^{-2}, open circuit voltage (V_{OC}) of 1.05 V, and fill factor (FF) of 0.79[9–12]. However, high efficiency c-PSCs rely strongly on mesoporous TiO$_2$ as an ETL, which requires a high temperature (450-500 °C) sintering process, making device manufacturing complicated and energy-intensive[13,14]. Meanwhile, the planar

c-PSCs without mesoporous scaffolds have drawn much interest due to their numerous advantages such as ease of device fabrication, potential flexibility, low fabrication costs and high scalability[15,16]. Despite these advantages, the planar c-PSCs suffer from the limited photovoltaic (PV) efficiencies due to the limited hole selectivity/extraction and inadequate interface contact between carbon electrode and perovskite film[17]. This has led to recent efforts being focused on fabricating c-PSCs with inorganic HTMs materials to obtain high device efficiency while achieving excellent stability. For instance, Yang et al.[18] employed a low-cost inorganic HTM (CuSCN) in planar c-PSCs and compared with Spiro-OMeTAD. The CuSCN based device showed an increased efficiency and improved stability as compared to the cells assembled using Spiro-OMETAD. The best device without encapsulation delivered a PCE of 14.7% while maintaining about 93% of its initial efficiency after being stored in a humid environment (55–70%) for 80 days. As such, exploring new materials that can be used as an efficient HTM for planar c-PSCs is an area of broad interest.

On the other hand, two-dimensional (2D) materials such as graphene derivatives, metal carbides or nitrides (MXene), transition metal dichalcogenides (TMDs) and elemental 2D materials have shown great promise not only to enhance the PV performance, but also play an important role in

[1]Queensland Micro- and Nanotechnology Centre, School of Environment and Science, Griffith University, Nathan, Brisbane, QLD 4111, Australia. [2]Australian Institute for Bioengineering and Nanotechnology, The University of Queensland, St Lucia, Brisbane, QLD 4072, Australia. [3]School of Chemistry and Physics, Faculty of Science, Queensland University of Technology, Brisbane, QLD 4001, Australia. [4]Centre for Materials Science, Queensland University of Technology, Brisbane, QLD 4001, Australia. [5]Queensland Micro- and Nanotechnology Centre, School of Engineering and Built Environment, Griffith University, Nathan, Brisbane, QLD 4111, Australia. ✉e-mail: y.zhong@griffith.edu.au; m.batmunkh@griffith.edu.au

device stabilities[19–22]. Besides improving the hole extraction and band alignment, 2D materials have been used as an interlayer in PV devices[20,23]. Specifically, single- and/or few-layer black phosphorus (BP), known as phosphorene, have recently attracted extensive attention as a potential HTM for PSCs due to their high carrier mobility, ambipolar conduction behaviour and tunable bandgap[24]. For example, Muduli et al.[25] reported the direct replacement of Spiro-OMeTAD using BP flakes with large lateral sizes (~1 μm) in PSCs. The outstanding hole selectivity of BP nanosheets was demonstrated by the device with BP nanosheets which exhibited significantly higher PCE (7.88%) than that of the devices without HTM (4%). Recently, the concept of using BP derivatives as an interlayer between perovskite layer and HTL has shown significant improvement in the hole transport due to the lowered injection barrier between the perovskite and HTL, and the favourable band energy alignment in conventional PSCs[26]. For instance, Chen et al.[27] inserted BP quantum dots (BPQDs) with an average size of only ~5.2 nm between PEDOT:PSS and perovskite layer, in which BPQDs acted as a hole extraction layer and improved the PV efficiency of PSCs. Furthermore, Macdonald et al.[26] employed phosphorene nanoribbons (50 nm-10 μm in length and 5-50 nm in width) with a variety of outstanding functional properties as an interlayer between PTAA and perovskite layer in inverted PSCs. They revealed that both calculated highest occupied molecular orbital (HOMO) level (~5.41 eV) and bandgap (~1.97 eV) of phosphorene nanoribbons make them highly suitable for use as a HTM in PSCs. The devices based on phosphorene nanoribbons achieved a PCE of >21%, whereas the best control cell displayed an efficiency of 19.60%. In a recent study by Liu et al.[28], an efficient hole injection interlayer was designed using fluorine functionalized BP nanosheets, which enabled the fabrication of high efficiency PSCs with PCEs of over 22%. However, the majority of these works have employed BP derivatives as the interlayer between HTM and perovskite layer in PSCs to improve and support the hole transportation. In addition, it should be noted that the lateral size of the BP flakes is expected to play critical roles in achieving excellent charge transportation and high surface coverage on the perovskite film.

In this work, we prepared few-layer large-area BP flakes using an electrochemical packed bed electrochemical reactor (PBER) and employed them as HTMs in planar c-PSCs. The device fabricated with BP flakes exhibited significantly increased PCE of over 15% with a high open circuit voltage (V_{OC}) of 1.082 V due to the suitable energy level alignment and enhanced hole extraction, while displaying reduced hysteresis. Moreover, BP flakes-based unencapsulated devices not only retained more than 93% of their stabilized PCEs after being stored in a humid environment (50-75% relative humidity (RH)) for 75 days, but also maintained 92% of their stabilized efficiencies with no further decay under the harsh testing conditions of 85°C temperature and 85% RH after 210 min.

Results and discussion
Preparation and characterization of large-area phosphorene
The electrochemical expansion of BP was carried out in a two-electrode PBER, in which a bed of bulk BP was pressed against a boron-doped diamond (BDD) working electrode and separated from a platinum (Pt) counter electrode with a glass fiber membrane (Fig. 1a). During the electrochemical expansion, tetrabutylammonium cations (TBA$^+$) were intercalated into the bulk BP layers, effectively increasing the interlayer spacing and creating the expansion of the BP crystal. The resulting expanded BP was exfoliated into nanosheets (eBP) using a mild sonication in dimethylsulfoxide (DMSO) for only 2 min due to the weakened interlayer van der Waals interaction caused by the presence of intercalants. The obtained eBP dispersion was centrifuged to remove the unexfoliated products followed by the solvent exchange process into isopropanol (IPA) for device fabrication. For the electrochemical expansion, various currents (−0.5 mA to −1.5 mA) were applied to optimize the eBP preparation to obtain the desired large lateral sizes (Supplementary Figs. 1 and 2). Based on the complete intercalation and the lateral size of the eBP flakes, −1 mA was selected as the optimum current value for the electrochemical expansion of BP. To compare the morphology

of the bulk BP and electrochemically expanded BP, the scanning electron microscopy (SEM) was performed. SEM image of the bulk BP (Fig. 1b) shows that the bulk BP had a typical closely packed layered structure. After the intercalation using optimized current of −1 mA (Fig. 1c), the packed layers of the bulk BP separated with increased interlayer spacing, making them ready to be exfoliated into individual or few-layer flakes.

The as-prepared eBP was characterized using a UV–vis spectroscopy, Raman spectroscopy, X-ray photoelectron spectroscopy (XPS) and atomic force microscopy (AFM). Two characteristic absorption peaks at wavelengths within the regions of 280-300 nm and 380-430 nm can be observed from the UV–vis spectrum of our eBP dispersion (Fig. 1d). It should be noted that previous experimental studies and theoretical density-functional theory (DFT) calculations showed that as the lateral size becomes larger, the characteristic peaks redshift toward their position in the 2D sheets[29]. This is in excellent agreement with our experimental finding as our eBP dispersion exhibits an absorption shoulder at wavelengths between 380 nm and 430 nm which is much higher wavelengths than those observed in literatures[29–31], indicating that our flake size is larger than these previous studies. To further confirm the oxidation states of our eBP, high resolution (HR) XPS spectra were scanned on our eBP sample and bulk BP. As illustrated in Fig. 1e, both bulk BP and eBP showed the P $2p_{3/2}$ and P $2p_{1/2}$ doublet at 129.9 eV and 130.9 eV, respectively, both of which can be associated to the characteristic signals of P–P bonds[32]. Moreover, a very small bump at a binding energy of around 134 eV can be observed from our eBP sample due to the slightly oxidized species of P[33]. This very low intensity peak indicates the successful production of eBP flakes with a minor oxidation.

Figure 1f displays the Raman spectra of bulk BP and eBP sample, both of which show three characteristic peaks centered at 353.8 cm^{-1}, 427.8 cm^{-1} and 456.2 cm^{-1} corresponding to the A^1_g, B_{2g} and A^2_g phonon modes, respectively[34]. The previous studies reported that the number of layers in BP nanosheets can be determined by the integrated intensity ratio of A^2_g and A^1_g peaks[35,36]. It was reported that the integrated intensity ratio of A^2_g/A^1_g is around 1.9 for the bulk BP, while the ratios of trilayer and bilayer phosphorene were calculated to be 3.5 and 7, respectively[36]. Based on our Raman spectra, the intensity ratio of A^2_g/A^1_g peaks for eBP sample was measured to be 3.4, suggesting it is in the region of trilayer BP. Furthermore, AFM was conducted to determine the thickness of the as-prepared eBP flakes. As demonstrated in Fig. 1g and Supplementary Fig. 3, the height profile measurement from the AFM image suggested that the thickness of our eBP flakes is mainly 1–3 nm, corresponding to 2−4 layers considering the thickness of single layer phosphorene is 0.53 nm[37]. The number of layers measured from the AFM analysis was consistent with our Raman results.

To investigate the structural morphology of the eBP, transmission electron microscopy (TEM), HRTEM and the corresponding energy-dispersive X-ray (EDX) elemental mapping images were performed. TEM image in Fig. 2a confirms the production of large-area flakes. Based on the statistical analysis of the lateral size and area distribution after examining ~200 flakes, it was revealed that the average lateral size of the eBP sheets is in the range of 2–4 μm (Fig. 2b) and the average lateral area is ~3–5 μm^2 (Fig. 2c) (see also Appendix in the Supplementary Information). From the TEM image depicted in Fig. 2d and the corresponding selected area electron diffraction (SAED) pattern (inset of Fig. 2d), it can be clearly seen that the eBP flakes are ultrathin single-crystal structure. As shown in Fig. 2e, the lattice fringe of our eBP sheet was measured to be 0.44 nm, which is ascribed to the (010) plane of crystalline BP[38,39]. As displayed in Fig. 2f, the high-angle annular dark-field-scanning transmission electron microscopy (HAADF-STEM) and EDX elemental mapping images indicate an uniform distribution of phosphorus atom on the eBP sample.

Characterization of perovskite films
The crystallinity and morphology of the perovskite film made from α-formamidinium lead triiodide (α-FAPbI$_3$) before and after using eBP flakes as HTL were evaluated using X-ray diffraction (XRD) and top-view SEM.
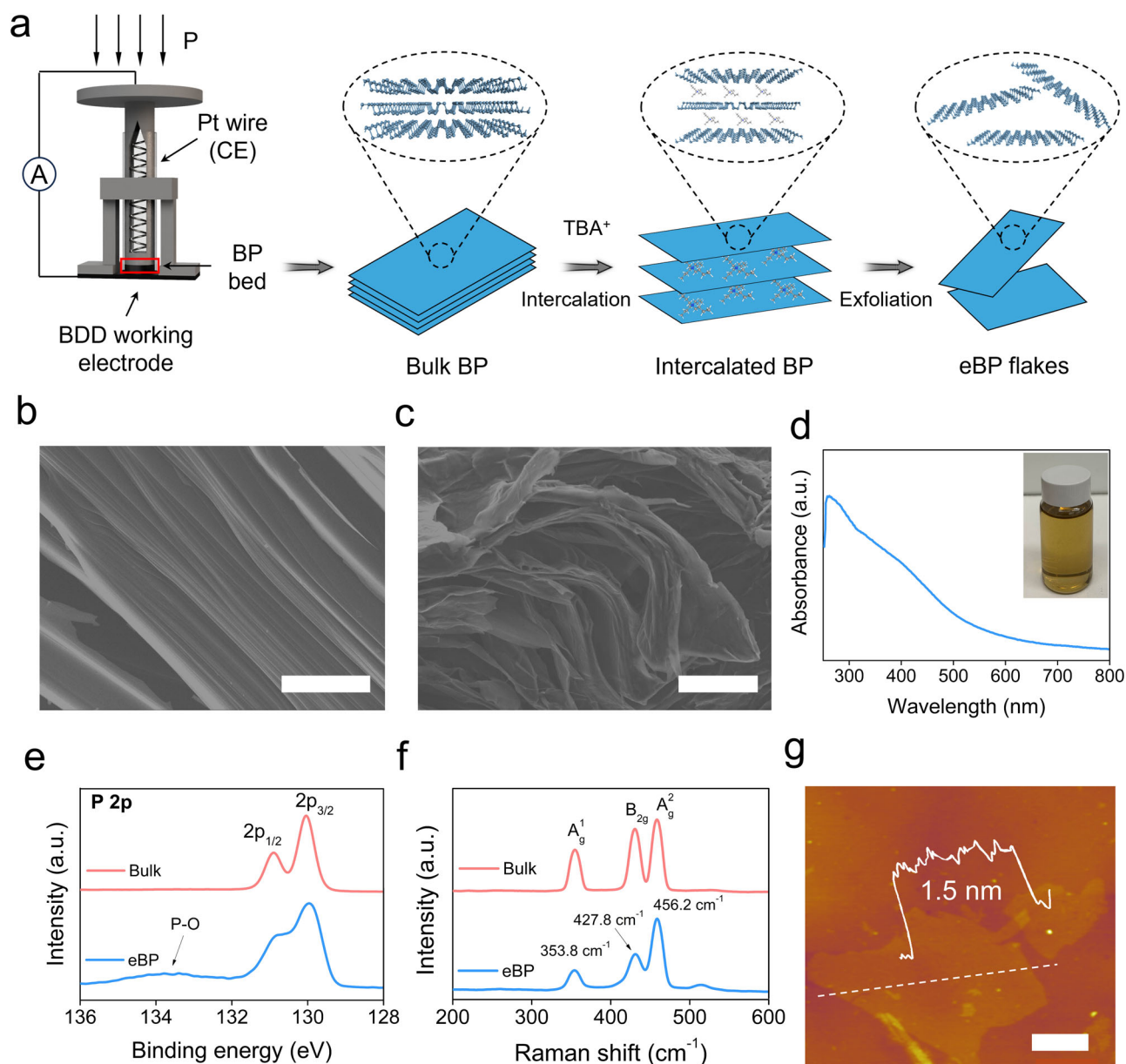
Fig. 1 | Preparation and characterization of large-area phosphorene flakes. **a** Schematic illustration of the electrochemical production of eBP. SEM images of **b** bulk and **c** expanded BP prepared using −1 mA (scale bar: 10 μm). **d** UV-vis spectrum of eBP dispersion (concentration: 0.083 mg mL^{-1}). **e** HR P 2p spectra and **f** Raman spectra of bulk BP and eBP. **g** AFM image of eBP flakes (scale bar: 1 μm).

From the XRD spectra shown in Fig. 3a, two strong peaks at 14.3° and 28.6° were observed in both films and can be assigned to the (001) and (002) crystal planes of α-FAPbI$_3$, respectively. Notably, after using eBP, a clear reduction in the intensity of the characteristic peak associated with PbI$_2$ at 12.7° suggests that eBP protects the surface of the α-FAPbI$_3$ film from the deterioration. It can be seen from the SEM images of the perovskite films with (Fig. 3b) and without (Fig. 3c) eBP HTL show that these two films have similar morphology displaying densely arranged grains with an average grain size of 1–2 μm. Importantly, the absence of any pinholes on the perovskite films is critical in achieving high device performances. It should be noted that since 2019, α-FAPbI$_3$ has been widely used as light harvesting perovskite materials and is one of the major perovskites for many record PV efficiencies[2,40–43], but the challenges are their instabilities. As such, improving the stability of this state-of-the-art perovskite would be of great value for the future development of PSCs and other devices based on α-FAPbI$_3$. Therefore, in this work, we focused on fabricating stable α-FAPbI$_3$ based thin films and devices.

To investigate the effect of eBP HTL on the perovskite films, XPS measurements were carried out on our α-FAPbI$_3$ perovskite films before and after depositing eBP flakes. It can be seen from the XPS Pb 4f core level spectra (Fig. 3d) that the perovskite and perovskite/eBP films present a similar Pb signal with a negligible metallic Pb (^{0}) peak with two main peaks of Pb 4f$_{7/2}$ and Pb 4f$_{5/2}$, indicating the absence of iodine vacancies in both films. To further determine the energy levels of the perovskite films with and without eBP HTL, UV-vis spectroscopy and ultraviolet photoelectron spectroscopy (UPS) were conducted. As shown in Fig. 3e, no significant changes were observed in the UV-vis absorption spectra of both perovskite films with and without eBP nanosheets. The bandgaps of the films were calculated to be around 1.52 eV, which is in excellent agreement with the reported values for α-FAPbI$_3$[44]. Detailed insights into the energy level alignments of perovskite films can be obtained from a combination of bandgap calculations (Fig. 3e inset) and UPS data analysis (Fig. 3f, g). In particular, the valence band maximum (VBM) and conduction band minimum (CBM) were slightly up-shifted for the perovskite film with eBP
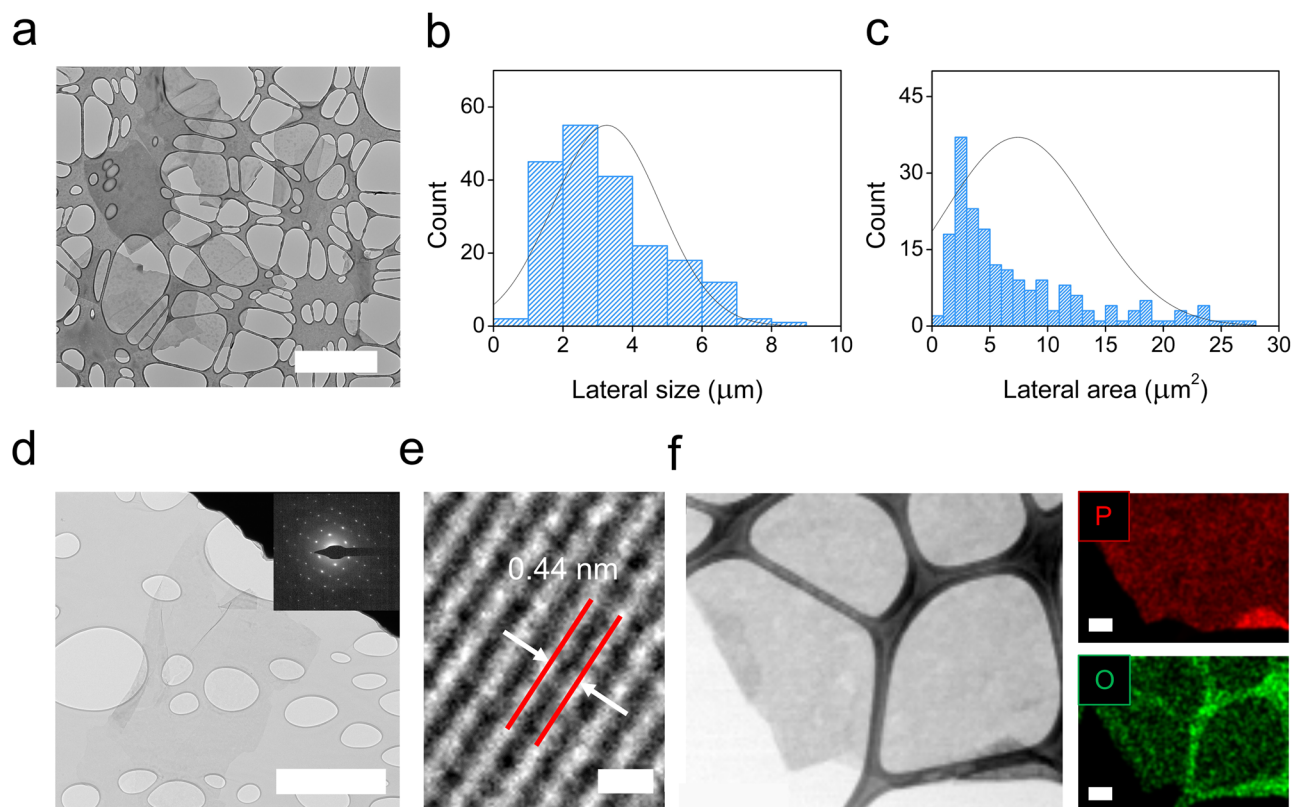
Fig. 2 | Microscopic analysis of large-area phosphorene flakes. a TEM image (scale bar: 2 μm), **b** lateral size histogram, **c** lateral area histogram, **d** TEM image (scale bar: 1 μm) and the corresponding SAED pattern, **e** HRTEM image (scale bar: 1 nm), **f** HAADF-STEM image and the corresponding EDX elemental mapping images (scale bar: 200 nm) of eBP flakes.

HTL, providing more suitable band energy alignment for each layer (component) of the devices including the ETL and carbon electrode. This favorable band energy alignment is expected to provide efficient hole selectivity and transportation (Fig. 3h), suppressing the charge recombination and reducing the hysteresis behaviour of the fabricated devices[45].

Device characterization and performance

PV characteristics of the c-PSCs with and without eBP HTL were investigated under standard air mass (AM) 1.5 illumination. Supplementary Fig. 4 displays the cross-sectional SEM image of the complete device with a layered structure of ITO/SnO$_2$/α-FAPbI$_3$/eBP/carbon. A summary of the detailed PV parameters including J_{SC}, V_{OC}, FF and PCE is presented in Fig. 4a–d. The photocurrent-voltage (J–V) curves of the best performing devices are shown in Fig. 4e. The best performing control device showed a maximum PCE of 13.48% with a J_{SC} of 21.46 mA cm^{-2}, a V_{OC} of 1.045 V and a FF of 60.06. In comparison, the devices using eBP nanosheets as HTL delivered a significantly improved PCE of 15.58% with the measured J_{SC} value of 22.89 mA cm^{-2}, V_{OC} of 1.082 V and FF of 62.85. To the best of our knowledge, the V_{OC} value obtained using our eBP based c-PSCs is the highest reported V_{OC} for c-PSCs without traditional HTMs (Supplementary, Table 1). We attribute this high V_{OC} value to the suitable band energy alignment of eBP with perovskite and carbon electrode. Furthermore, the considerable PCE enhancement was mainly derived from the improved J_{SC} and V_{OC}. We postulate that the well-aligned band energy and hole extraction ability of eBP nanosheets lead to efficient hole transfer from the perovskite layer to the carbon electrode[46].

External quantum efficiency (EQE) spectra of the devices with and without eBP HTL are depicted in Fig. 4f. The integrated J_{SC} values from the EQE spectra were 20.67 mA cm^{-2} and 21.44 mA cm^{-2} for the control and eBP based devices, respectively, both of which are in the range of the corresponding statistical distributions of the measured J_{SC} (see Fig. 4b). To

investigate the charge extraction properties of the eBP, steady-state photoluminescence (PL) measurements were conducted on the perovskite films with and without eBP HTL. As shown in Fig. 4g, the PL of the perovskite film with eBP is considerably quenched as compared to the control perovskite film, suggesting efficient hole extractions at the interface of perovskite/eBP.

Hysteresis observed during reverse and forward J–V scan directions is one of the critical behaviours for solar cells. A poor interfacial contact has been found to be responsible for severe hysteresis behaviour of c-PSCs due to the unbalanced electron and hole extraction rates at the interfaces of perovskite/ETL and perovskite/HTL or perovskite/carbon[47]. To further explore the charge extraction properties of the fabricated devices, we compared the hysteresis behaviour of the control (Fig. 5a) and eBP (Fig. 5b) based c-PSCs by scanning in both reverse (from +1.5 V to –0.1 V) and forward (from –0.1 V to +1.5 V) scan directions. It can be clearly observed from Fig. 5a and b that the device fabricated using eBP HTL showed a reduced hysteresis in comparison to the control c-PSC without any HTL. To quantify the degree of hysteresis behaviour of the devices, the following Eq. (1) can be used for defining the hysteresis index (HI)[48].

$$HI = \frac{PCE_{reverse} - PCE_{forward}}{PCE_{reverse}} \tag{1}$$

It was found that the HI was significantly decreased from 0.282 to 0.187 after using eBP HTL, indicating that eBP flakes improve the interfacial contact of perovskite/carbon. This hysteresis improvement observed when using eBP may also be due to the suppression of ion migrations in the presence of eBP on the perovskite films[49]. These results clearly demonstrate the excellent hole transporting properties of eBP nanosheets.

Moreover, it is well known that the J–V curves of PSCs should be scanned not only in both scan directions, but they should also be recorded at
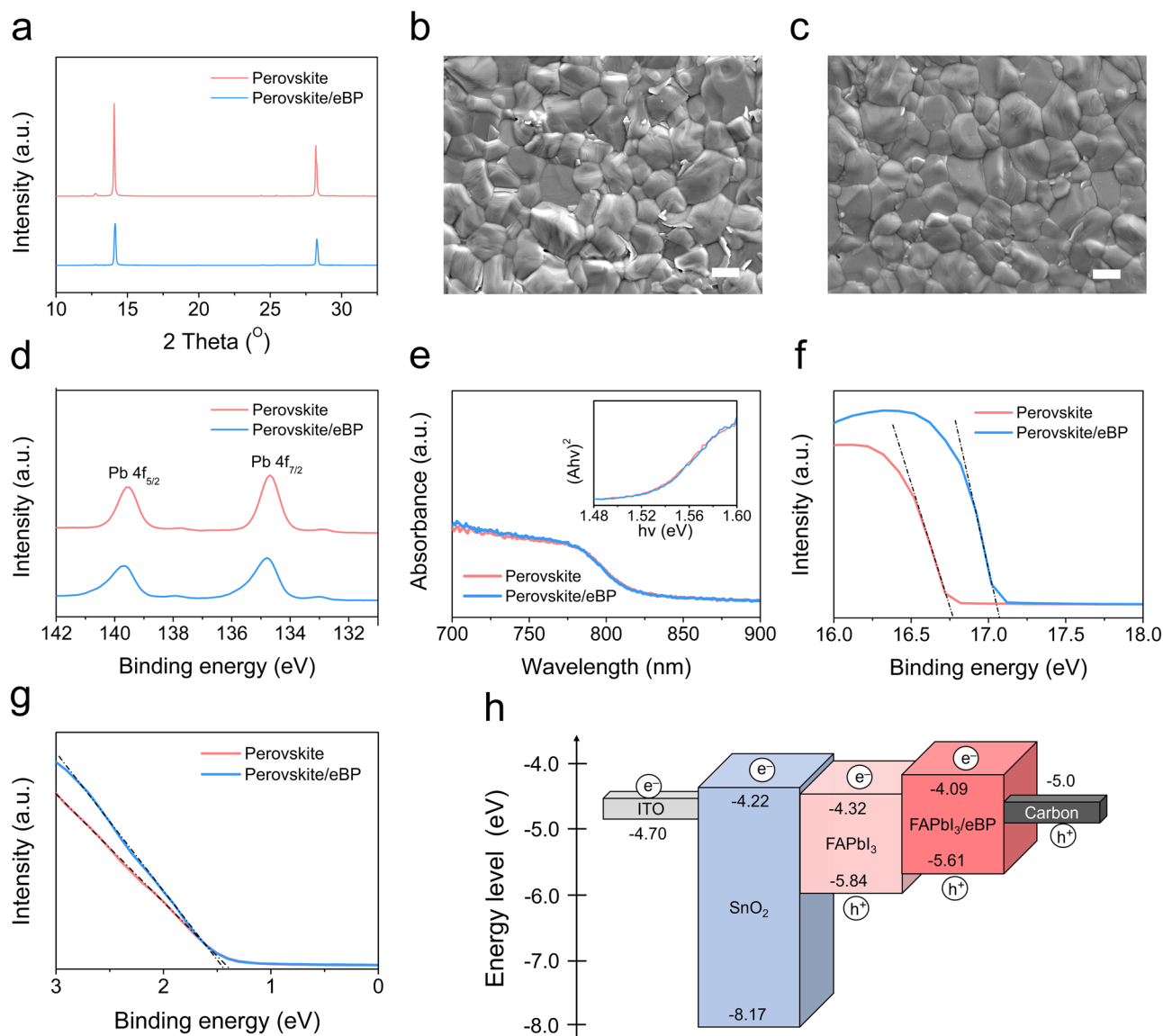
Fig. 3 | Characterizations of perovskite films with and without eBP. a XRD patterns of the perovskite films with and without eBP. Top-view SEM images (scale bar: 1 μm) of **b** perovskite film and **c** eBP deposited perovskite film. **d** HR Pb 4 f core level XPS spectra of perovskite films with and without eBP. **e** UV–vis spectra (inset shows Tauc plot), (**f** and **g**) UPS spectra of the perovskite films with and without eBP. **h** The measured energy-level values of each component used in the fabrication of PSCs.

different scan rates to demonstrate the device performance[50–52]. For this reason, J-V curves of the eBP based devices were obtained at different scan rates ranging from 50 to 300 mV s^{-1}. As depicted in Fig. 5c, there was almost no change observed in all PV parameters, indicating reasonably stable PV characteristics of our eBP based device.

Device stability

High efficiency and stable photovoltaic devices should withstand against harsh testing conditions in alignment with the International Sumit on Organic Photovoltaic Stability (ISOS) protocols, specifically ISOS-D-2I and ISOS-L-2[53]. We conducted long-term stability tests on our control and eBP based devices in ambient air without encapsulation under a RH of 50-75% for 75 days. It can be seen from Fig. 5d that both devices maintained >93% of their stabilized PCEs after 75 at a RH of 50-75%. It is well established that c-PSCs are highly stable in ambient conditions. Therefore, this work demonstrates that the use of eBP in c-PSCs does not degrade the device stabilities in ambient conditions[54,55]. Interestingly, both devices show initial enhancement of 21%-22% in the PCEs in the first eight days, followed by PCE stabilization. Recently, it was reported that due to the exposure to

humid atmosphere, α-FAPbI$_3$ perovskite transforms to δ-phase FAPbI$_3$ at the perovskite/carbon interface which forms an α/δ-phase junction, leading to the PCE improvement during the initial aging period[44]. It should be noted that all PV performances of the devices presented in this work including statistical distributions of PCE, J_{SC}, V_{OC} and FF were sourced from the measurements of 10th day.

We further tested the devices under harsh conditions such as 85% RH (at room temperature) and heating at a temperature of 85 °C with 85% RH. It is worth noting that the stability measurements were carried out continuously on the same devices used for previous long-term stability tests over 75 days. As shown in Fig. 5e, both devices were still able to retain more than 92% of their stabilized PCEs after being stored at a RH of 85% at room temperature. As shown in Fig. 5f, 14% decay in the PCE was observed for the control device due mainly to the decreased J_{SC} and FF values (Supplementary Fig. 5), caused by the deterioration of perovskite films. Surprisingly, eBP based device exhibited excellent heat stability with no further reduction after 210 min under combined testing conditions of 85 °C and 85% RH, which can be attributed to the double protection of eBP HTL and carbon electrode, minimizing the water penetration into the perovskite films. It has
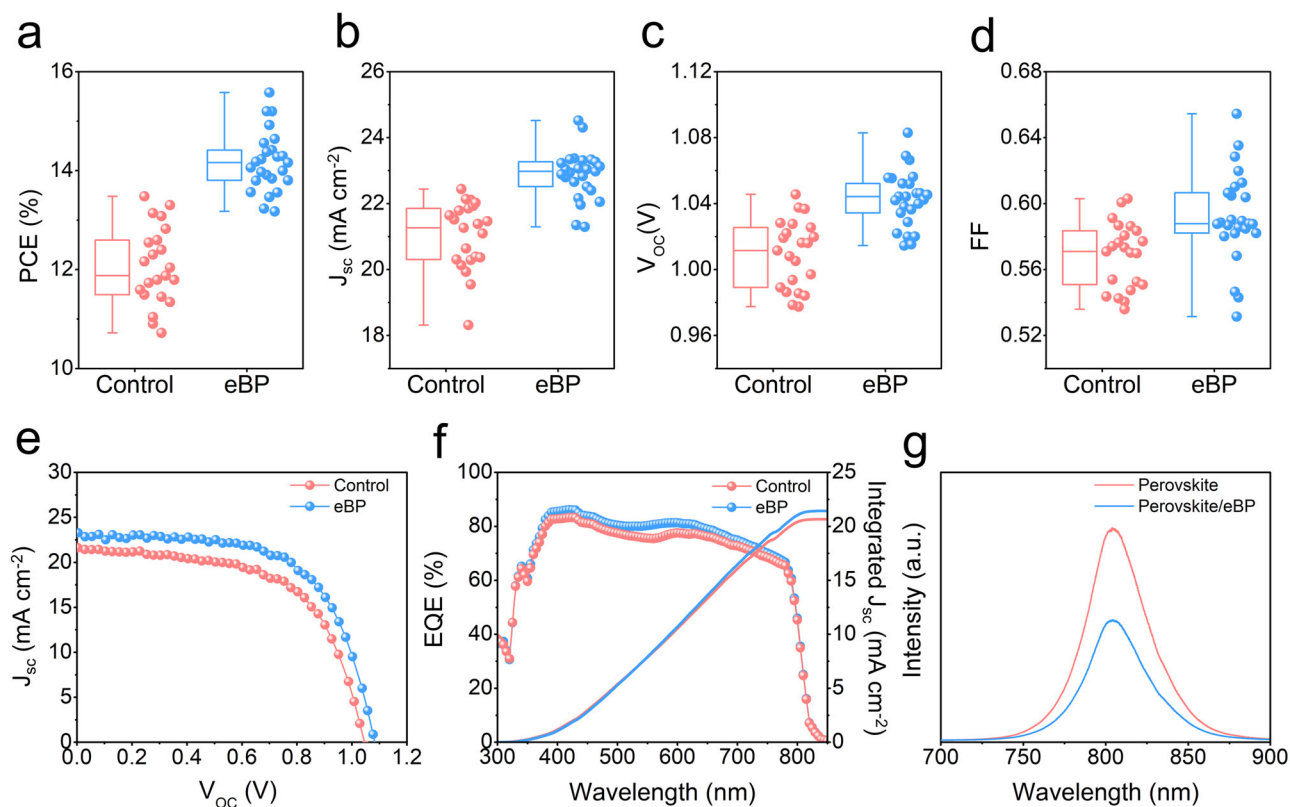
Fig. 4 | PV performances of carbon-based PSCs with and without eBP flakes. Statistical distribution of **a** PCE, **b** J_{SC}, **c** V_{OC} and **d** FF of c-PSCs without any HTL (control) and with eBP HTL (eBP). **e** J-V characteristics and **f** EQE spectra of the best performing control and eBP based devices. **g** PL spectra of the perovskite films with and without eBP HTL.

been reported in previous studies that a pristine BP surface is relatively hydrophobic[33,56], which is expected to block the penetration of water molecules into the perovskite film. To confirm this, the water contact angles of the perovskite films with and without eBP were measured (Supplementary Fig. 6). The contact angle of the perovskite film with eBP was measured to be 70.42°, which is much higher than that of the perovskite film without eBP (55.38°). This presence of eBP enhanced the film hydrophobicity and increased the moisture resistance. The research on BP hydrophobicity has been around for nearly a decade[56]. To the best of our knowledge, we were the first to demonstrate the applicability and benefits of using hydrophobic BP layers in solar cells[48].

Theoretical calculations

Density functional theory (DFT) calculations were performed to further investigate the structural and electronic properties of the perovskite/eBP using the VASP package. The optimized Becke88 functional (optB88) including the non-local vdW-DF correlation (optB88-vdW) was used for all the calculations due to its appropriateness in describing the structural parameters and binding energies for a wide range of 2D materials as reported in our earlier benchmark study[57]. Besides, optB88-vdW functional also works well for halide perovskite materials and is widely used to study FAPbI$_3$-based heterostructures[58,59]. BP(010) and FAPbI$_3$(001) surfaces were used to model the structures of eBP and perovskite, respectively, according to their experimental characterizations (Figs. 2, 3). Since the orientation of cation inside the PbI$_6$ cage was reported to influence the electronic properties of the hybrid halide perovskite[60,61], the influence of the FA orientation on the stability of the FAPbI$_3$ (001) surface was investigated and the most stable structure was chosen for our DFT calculations (details are presented in the Supplementary Table 2 and Fig. 7). Based on the computational optimized lattice parameters, the low lattice mismatch heterostructures including periodic (1×5) slabs of FAPbI$_3$(001) and (2×7) slabs of BP(010)

were successfully built to represent the structure of perovskite/eBP (more details in the Supplementary Information).
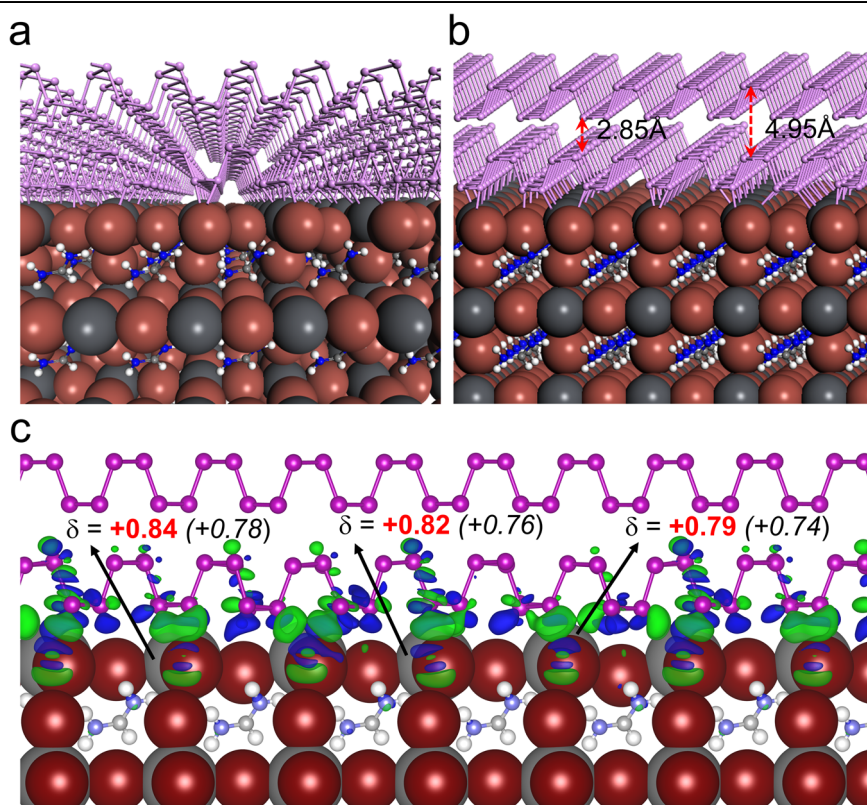
Firstly, the interaction between BP layers and FAPbI$_3$ perovskite was investigated. The computed adhesion energies of BP films with different phosphorene thickness on the perovskite support are presented in Supplementary Table 3. The adhesion energy of a monolayer phosphorene and perovskite was −1.59 eV and decreased significantly when the number of BP layers increased, suggesting that the phosphorene layers at the further proximity from the interface only interacts weaker with the perovskite. Indeed, the differential adhesion energies for 3-layers and 4-layers of phosphorene on perovskite was −0.41 eV and −0.43 eV, respectively, which is the same as the cohesive energy of a pure phosphorene[62,63]. The strong perturbation from phosphorene to perovskite is still considered as an effect for the 2-layers BP/perovskite since the differential adhesion energy for this heterostructure is -0.64 eV, much stronger than the cohesive energy of a pure phosphorene. This observation is consistent with the confinement of interfacial interaction in heterostructure systems within 3 atomic layers above the interface reported recently[64,65].

Next, the Bader charge analysis was carrier out to evaluate the charge transfer between the BP and perovskite, which is an important factor contributing to the stability of the heterostructure[62,64,66]. As can be seen from Supplementary Table 3, there is a transfer of 0.31 electrons from monolayer BP to perovskite. This charge transfer is stronger for the thicker BP layers on perovskite, with 0.65 electron is transferred from the bilayer BP to the perovskite. This charge transfer remains the same rate for 3-layers and 4-layers of BP on perovskite. As the representative structure, the optimized bilayer BP/perovskite structure is shown in Fig. 6a, b. It can be seen that there are strong covalence bonds between P atoms (from phosphorene) and Pb and I atoms of the perovskite at the interface. Due to this strong interaction, the structure of perovskite is stabilized against the influence of moisture and other species such as O$_2$ molecule and OH radical, as was also reported for
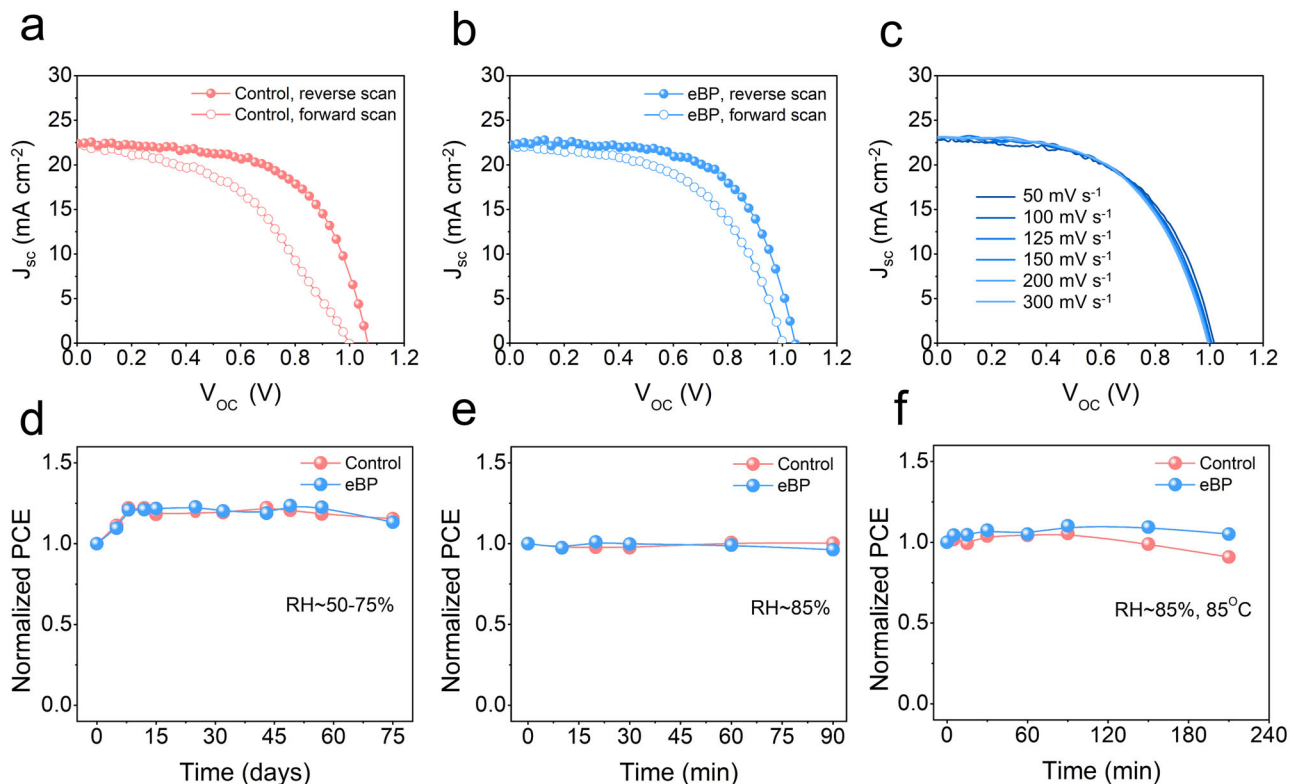
Fig. 5 | Device stability and hysteresis tests. J–V characteristics of the **a** control and **b** eBP based devices measured in the reverse and forward scan directions. **c** J–V characteristics of the eBP based device measured at different scan rates. Stability tests of unencapsulated devices with and without eBP HTL **d** aged in ambient air with 50-75% RH for 75 days, **e** tested under 85% RH for 90 min (room temperature), **f** aged at 85 °C with 85% RH for 210 min. Notably, the stability measurements were carried out continuously on the same devices for these three tests.

Fig. 6 | Theoretical investigations of phosphorene-perovskite interfaces. a, **b** Two different views of the optimized structure of 2-layers BP on $FAPbI_3$. **c** The charge density difference plot for $FAPbI_3$/BP, wherein the depleted/excess charge densities are indicated by green/blue colour regions. Computed Bader charges for Pb atoms at the $FAPbI_3$/BP interface are presented in red numbers, while their corresponding values on bare $FAPbI_3$ perovskite surface are shown in parentheses.

perovskite covered by graphene layers[59]. The charge density difference for the interaction between bilayers phosphorene and $FAPbI_3$ perovskite is displayed in Fig. 6c. It can be seen that the charge transfer between BP and perovskite induces more positive charge on Pb atoms located at the interface as compared to the pure perovskite structure. As reported in earlier studies[67,68], the charge withdrawal to induce more positive charge on an atom results in the XPS shift of that atom to higher binding energies[69], which is consistent with the slight shift (to higher binding energies) in the HR Pb $4f$ core level observed experimentally in Fig. 3d.

From these observations, it is suggested that the optimized thickness of BP should be two or three atomic layers to maximize the charge transfer between BP to enhance the stability of the perovskite phase. Thicker phosphorene layers might not be stable due to their weak adhesion energies on the perovskite. It has also been reported by Cai et al.[62] that the bandgap, band alignment, work function, and carrier effective masses of BP films are dependent on the number of BP layers; and a few-layer BP (less than 4 layers) is likely to perform better than monolayer phosphorene and can lead to more efficient hole injection and transport across the contact. Since the thickness of our eBP films was mainly 1-3 layers (Supplementary Fig. 3), the understanding on the electronic properties of our eBP/perovskite heterostructures further support their significant enhancement in hole selectivity and transportation as observed in our experimental results.

In summary, we have employed the electrochemically synthesized ultrathin eBP flakes with large lateral size as a HTM in c-PSCs and investigated their electronic and PV performances. By employing eBP flakes as HTL, suitable band energy alignments were obtained, leading to the enhanced hole selectivity and transportation. These improvements were found to be responsible for the reduced charge carrier recombination and the negligible hysteresis behaviour of the planar c-PSCs. As a result, our c-PSCs with eBP HTL achieved significantly improved PCEs of over 15% with a remarkably high V_{OC} of 1.082 V which is the highest reported value for c-PSCs without traditional HTMs. More importantly, the unencapsulated c-PSCs with eBP flakes exhibited excellent stabilities under various harsh testing conditions including high temperature and humidity due to the combined protection of hydrophobic eBP HTL and carbon electrode.

Methods

Materials
Unless otherwise stated, all chemicals were purchased from Merck. Bulk BP (99.998% pure) was purchased from Smart Elements. Indium-doped tin oxide (ITO) glass substrates (1.5 cm × 2 cm) were purchased from Ossila Ltd. Tin oxide (SnO_2) colloidal solution (15 wt% in water) was purchased from Alfa Aesar. Lead iodide (PbI_2) (ultra dry, 99.999%, metal basis) was purchased from Thermo Fisher. Formamidinium iodide (FAI) and methylammonium iodide (MACl) were purchased from Xi'an Yuri Solar Co.,Ltd. Carbon paste was obtained from Dyenamo AB.

Synthesis of α-FAPbI3
α-FAPbI$_3$ black powder was synthesized by mixing 3.36 g FAI with 9 g PbI_2 (1:1 molar ratio) in 11 mL of 2-ME in a 50 mL vial by stirring. The mixed solution was heated to 125 °C in an oil bath and stirred for 60 min. Subsequently, the black precipitate was filtered using a filter paper (Whatman) without cooling to room temperature. The filtered α-FAPbI$_3$ was heated on a hot plate at 150 °C in air for 30 min and then left overnight in a vacuum desiccator.

Preparation of eBP flakes
eBP flakes were synthesized in a PBER under constant current[70]. Briefly, 20 mg bulk BP was pressed against a conductive BDD (Diaccon GmBH) working electrode under an applied pressure (0.5 kg top load) and separated from a Pt counter electrode using a glass fiber membrane (GF/B; Whatman). A Pt wire (0.25 mm diameter) with a length of 33 cm (purity 99.99%; Goodfellow) was used. 5 mL non-aqueous electrolyte of 0.1 M tetra-buthylammonium (TBA) hydrogensulfate in DMSO was pipetted into the reactor. A Gamry electrochemical workstation (Interface 1010E) was

employed for the galvanostatic charging (GC) with the limiting voltage set at −8.0 V. After complete intercalation, the expanded BP was further exfoliated and dispersed in DMSO via ultrasonication for 2 min. The as-prepared eBP dispersion was centrifuged at 12,000 rpm for 10 min. The precipitates were collected and rinsed/washed for three times in an anhydrous isopropyl alcohol (IPA) by centrifuging at 12,000 rpm for 10 min each, followed by re-dispersing in IPA via ultrasonication for 2 min. After re-dispersing the precipitates in IPA, another centrifugation at 8000 rpm for 10 min was proceeded and supernatant was collected for device fabrication. The as-prepared eBP sample was stored in a N_2-filled glovebox. All the steps including electrochemical expansion, centrifugation and sonication were carried out in ambient conditions. Sample preparation for Raman, XPS and AFM characterization was carried out in the N_2 glovebox.

Device fabrication
ITO glass substrates with a sheet resistance of 15 Ω sq^{-1} were sonicated in detergent, distilled water, acetone, and isopropanol for 15 min each before being treated with ultraviolet (UV) ozone for 10 min. A thin SnO_2 film was deposited by spin coating a dilute SnO_2 solution (2.67% in water) onto the ITO at 3000 rpm for 30 s, followed by annealing at 150 °C for 30 min in an ambient atmosphere. After cooling to room temperature, the substrates were again treated with UV ozone for 10 min before being transferred to the N_2 glovebox. The perovskite precursor solution was prepared by dissolving 1.4 M α-FAPbI$_3$ powder with 35 mol% MACl, and 3.8 mol% methylene-diammonium chloride ($MDACl_2$) in a mixed solvent of dimethylformamide (DMF) and DMSO (8:1 v/v). Then, the perovskite solution was spin-coated onto SnO_2 at 1000 rpm for 10 s and 5000 rpm for 15 s. During the spinning, 800 μL diethyl ether was dripped onto the substrate. The as-deposited perovskite films were annealed at 125 °C for 60 min in ambient conditions with controlled humidity of 35–40%. Subsequently, the substrates were transferred to the glovebox. For the fabrication of eBP treated perovskite films, eBP solution (in IPA solvent) was spin coated on top of the perovskite films at 2000 rpm for 30 s, followed by annealing at 100 °C for 2 min. Finally, 27 μm carbon electrode was deposited by doctor blading carbon paste and then annealed at 120 °C for 15 min.

Materials characterizations
SEM images were obtained using a field-emission-scanning electron microscope (JOEL 7100 F). The optical absorbance spectra were obtained using a UV–vis spectrometer (Shimadzu UV-2600). Raman spectra were acquired using a WITec alpha300 RA + S with a 40× objective. XPS data were acquired using a Kratos Axis ULTRA X-ray Photoelectron Spectrometer incorporating a 165 mm hemispherical electron energy analyzer. The incident radiation was monochromatic Al Kα X-rays (1486.6 eV) at 225 W (15 kV, 15 mA). Base pressure in the analysis chamber was 1.0×10^{-9} torr and during sample analysis 1.0×10^{-8} torr. AFM was performed in air using Asylum Research Cypher S with Asylum Research software, operating in standard tapping mode configuration using AIR cantilever holder. TEM measurements were also performed using a HITACHI HT7700-A EDS for the statistical analysis of the size and area distribution and a FEI Titan Themis for the selected area electron diffraction (SAED) images. STEM imaging and EDX elemental mapping were carried out also on a FEI Titan Themis S-TEM instrument. The STEM probe was aberration-corrected, enabling sub-angstrom spatial resolution, and HAADF images were obtained. Water contact angle measurements were carried out on a Drop Shape Analyzer (Biolin ThetaFlex). The drop size was 5 μL. Recorded contact duration was 30 s.

Film and device characterization
The cross-sectional SEM images of the device and the top-view SEM images were obtained using a field-emission-scanning electron microscope (JOEL 7100F). XPS and UPS were obtained using a Kratos Axis Supra$^+$ using an Al Kα (λ = 1486.6 eV) and He I (λ = 21.22 eV) source, respectively. The crystal structures of perovskite films were recorded using a X-ray diffraction (the Bragg-Bentono geometry) on a Rigaku Smartlab diffractometer equipped

Article

with a 9 kW Cu rotating anode operating at 45 kV and 200 mA with a scanning range from 5° to 55° (2θ). UV-vis spectra were recorded on an Agilent 8453 UV-visible spectrophotometer. The steady-state PL emissions were measured at 803 nm using 532 nm excitation laser source on a Renishaw QONTOR InVia Raman Microscope. EQE was conducted using a quantum efficiency system (IQE 200B, Newport) under AC mode. J-V characteristics were performed in ambient air using a Ossila J–V test system under 1 sun illumination (AM 1.5 G, 100 mW cm^{-2}) with a scan rate of 125 mV s^{-1}. The illumination intensity was 100 mW cm^{-2} from the solar simulator (Sun 2000, Abet Technologies), which was calibrated against a National Renewable Energy Laboratory (NREL) certified standard 2 cm × 2 cm silicon photodiode. All the measurements were performed at room temperature without encapsulation. The active area of the tested solar cells was defined by a metal mask with an aperture area of 0.022 cm^2.

Theoretical calculations

All DFT calculations were performed using a plane-wave basis set with a cut-off kinetic energy of 500 eV and the projector-augmented wave (PAW) scheme[71] implemented in the ab-initio total-energy and molecular-dynamics program VASP (Vienna ab-initio simulation program) developed at the Fakultät für Physik of the Universität Wien[72,73]. To take the van der Waals interaction in all the structures (perovskite, BP, and perovskite/eBP) into account, we employed the optimized Becke88 functional (optB88) coupled with the non-local vdW-DF correlation (optB88-vdW) developed by Klimeš et al.[74,75]. Earlier studies reported that this choice of functional described reasonably well the lattice constant and binding energies across various 2D materials, also including phosphorene with thicknesses from mono to few layers[57,62]. Furthermore, the use of optB88-vdW function is also appropriate for DFT studying on FAPbI$_3$ materials, as was widely used to investigate the structures and electronic properties of FAPbI$_3$ and transition metals/graphene heterostructures[58,59]. Indeed, the optimized lattice parameters obtained for an 8-atoms unit cell of bulk BP using the optB88-vdW function in our DFT calculations are a = 3.32 Å; b = 4.50 Å and c = 10.73 Å, which are consistent with earlier computational studies[62,76] and experimental data (a = 3.31 Å; b = 4.37 Å and c = 10.48 Å)[77,78]. The optimized lattice constant for cubic phase α-FAPbI$_3$ using the optB88-vdW function is a = 6.391 Å, in excellent agreement with the experimental value of 6.362 Å[79]. Besides, the bandgap of 1.58 eV was obtained for α-FAPbI$_3$ in our study, which is 0.1 eV larger than the reported experimental value of 1.48 eV[80], justifying the appropriateness of this function for DFT studies in our study.

The structure of perovskite FAPbI$_3$ film was modelled using the 5 layers PbI$_2$-terminated FAPbI$_3$(0001) surface, which was reported as the most stable exposed surface of FAPbI$_3$[59,81]. eBP films were modelled using the BP(010) surface with thicknesses varying from mono to 4 atomic layers, according to the presence of the (010) plane of crystalline BP in eBP flake characterization (main text, Fig. 1e). Based on the obtained optimized lattice parameters, the heterostructures between the FAPbI$_3$ and eBP phases was built composing of the periodic (1 × 5) slabs of FAPbI$_3$(001) and (2 × 7) slabs of BP(010) to represent the structure of perovskite/eBP. The lattice mismatches between those two phases for this heterostructure were only 3.9% and 4.8% along the x and y direction. A k-point grid density of 4×2×1 was used to sample the Brillouin zone for all the calculations on perovskite/eBP systems. Geometries were fully relaxed with the convergence criteria for total energy and interatomic forces was set to 10^{-6} eV per unit cell and 0.01 eV Å^{-1}, respectively. To understand the electronic properties of eBP/FAPbI$_3$ interfacial structure and the range of the interfacial interaction, we computed the adhesion energies (ΔE_{adh}) for the eBP overlayer films on FAPbI$_3$ with different eBP thicknesses (one, two, three, and four overlayers). The Bader charges of all atoms in those structures were also computed using the approach by Henkelman et al.[82,83].

Optimization of applied current for electrochemical BP expansion

To optimize the currents for electrochemical BP expansion, a series of constant currents, ranging from −0.5 mA to −1.5 mA, were applied in a PBER. When the currents were over −1 mA, BP were fully expanded, while the currents of −0.5 mA and −0.75 mA were insufficient for the expansion (Supplementary Fig. 1). To choose one of the currents among −1 mA, −1.25 mA and −1.5 mA, around 240 measurements of lateral sizes and areas were performed using a TEM for each current. Histograms of the lateral measurements (Supplementary Fig. 2) showed that when the higher currents of −1.25 mA and −1.5 mA were applied, the lateral size and area of eBP nanosheets were smaller, which is possibly due to the strong expansion, leading to the damage of the flakes. Hence, the current of −1 mA was selected as the optimum current for the electrochemical expansion considering the complete intercalation and large size BP nanosheets.

Reporting summary

Further information on research design is available in the Nature Research Reporting Summary linked to this article.

Data availability

The data of this study are available from the corresponding author upon reasonable request.

References

1. NREL, *Best Research Efficiency chart* **2024**, (Accessed on 11 January 2024).
2. Park, J. et al. Controlled growth of perovskite layers with volatile alkylammonium chlorides. *Nature* **616**, 724–730 (2023).
3. Prasanna, R. et al. Design of low bandgap tin–lead halide perovskite solar cells to achieve thermal, atmospheric and operational stability. *Nat. Energy* **4**, 939–947 (2019).
4. Rong, Y. et al. Challenges for commercializing perovskite solar cells. *Science* **361**, eaat8235 (2018).
5. Bati, A. S. R. et al. Next-generation applications for integrated perovskite solar cells. *Commun. Mater.* **4**, 2 (2023).
6. Liu, X. et al. Stabilization of photoactive phases for perovskite photovoltaics. *Nat. Rev. Chem.* **7**, 462–479 (2023).
7. Cao, Y. et al. Ligand modification of Cu$_2$ZnSnS$_4$ nanoparticles boosts the performance of low temperature paintable carbon electrode based perovskite solar cells to 17.71. *J. Mater. Chem. A* **8**, 12080–12088 (2020).
8. Liu, S. et al. 17% efficient printable mesoscopic PIN metal oxide framework perovskite solar cells using cesium-containing triple cation perovskite. *J. Mater. Chem. A* **5**, 22952–22958 (2017).
9. Liu, S. et al. Highly oriented MAPbI3 crystals for efficient hole-conductor-free printable mesoscopic perovskite solar cells. *Fund. Res.* **2**, 276–283 (2022).
10. Bogachuk, D. et al. Perovskite solar cells with carbon-based electrodes - quantification of losses and strategies to overcome them. *Adv. Energy Mater.* **12**, 2103128 (2022).
11. Li, L. et al. Moisture induced secondary crystal growth boosting the efficiency of hole transport layer-free carbon-based perovskite solar cells beyond 19.5%. *Adv. Funct. Mater.* **34**, 2308428 (2024).
12. Xiang, J. et al. A polymer defect passivator for efficient hole-conductor-free printable mesoscopic perovskite solar cells. *Adv. Funct. Mater.* **33**, 2300473 (2023).
13. Bogachuk, D. et al. Low-temperature carbon-based electrodes in perovskite solar cells. *Energy Environ. Sci.* **13**, 3880–3916 (2020).
14. He, S. et al. Carbon-based electrode engineering boosts the efficiency of all low-temperature-processed perovskite solar cells. *ACS Energy Lett.* **4**, 2032–2039 (2019).

15. Su, H. et al. Carbon film electrode based square-centimeter scale planar perovskite solar cells exceeding 17% efficiency. *Mater. Sci. Semicond. Process* **107**, 104809 (2020).

16. Liu, X. et al. 17.46% efficient and highly stable carbon-based planar perovskite solar cells employing Ni-doped rutile TiO2 as electron transport layer. *Nano Energy* **50**, 201–211 (2018).

17. Li, S. et al. Hole transport layer-free carbon-based perovskite solar cells with high-efficiency up to 17.49% in air: From-bottom-to-top perovskite interface modification. *Chem. Eng. J.* **455**, 140727 (2023).

18. Yang, Y. et al. Spiro-OMeTAD or CuSCN as a preferable hole transport material for carbon-based planar perovskite solar cells. *J. Mater. Chem. A* **8**, 12723–12734 (2020).

19. Suragtkhuu, S. et al. Graphene-like monoelemental 2D materials for perovskite solar cells. *Adv. Energy Mater.* **13**, 2204074 (2023).

20. Bati, A. S. R., Batmunkh, M. & Shapter, J. G. Emerging 2D layered materials for perovskite solar cells. *Adv. Energy Mater.* **10**, 1902253 (2020).

21. Bati, A. S. R. et al. Cesium-doped Ti3C2Tx MXene for efficient and thermally stable perovskite solar cells. *Cell Rep. Phys. Sci.* **10**, 100598 (2021).

22. Gholipoor, M., Solhtalab, N. & Mohammadi, M. H. High-performance parallel tandem MoTe2/perovskite solar cell based on reduced graphene oxide as hole transport layer. *Sci. Rep.* **12**, 20455 (2022).

23. Liang, M. et al. Improving stability of organometallic-halide perovskite solar cells using exfoliation two-dimensional molybdenum chalcogenides. *npj 2D Mater. Appl.* **4**, 40 (2020).

24. Batmunkh, M., Bat-Erdene, M. & Shapter, J. G. Black phosphorus: synthesis and application for solar cells. *Adv. Energy Mater.* **8**, 1701832 (2018).

25. Muduli, S. K. et al. 2D black phosphorous nanosheets as a hole transporting material in perovskite solar cells. *J. Power Sources* **371**, 156–161 (2017).

26. Macdonald, T. J. et al. Phosphorene nanoribbon-augmented optoelectronics for enhanced hole extraction. *J. Am. Chem. Soc.* **143**, 21549–21559 (2021).

27. Chen, W. et al. Black phosphorus quantum dots for hole extraction of typical planar hybrid perovskite solar cells. *J. Phys. Chem. Lett.* **8**, 591–598 (2017).

28. Liu, T. et al. Fluorinated black phosphorene nanosheets with robust ambient stability for efficient and stable perovskite solar cells. *Adv. Funct. Mater.* **32**, 2106779 (2022).

29. Bat-Erdene, M. et al. Efficient and fast synthesis of few-layer black phosphorus via microwave-assisted liquid-phase exfoliation. *Small Methods* **1**, 1700260 (2017).

30. Ahmed, T. et al. Degradation of black phosphorus is contingent on UV–blue light exposure. *npj 2D Mater. Appl.* **1**, 18 (2017).

31. Guo, Z. et al. From black phosphorus to phosphorene: basic solvent exfoliation, evolution of raman scattering, and applications to ultrafast photonics. *Adv. Funct. Mater.* **25**, 6996–7002 (2015).

32. Zhang, L., Ding, L.-X., Chen, G.-F., Yang, X. & Wang, H. Ammonia synthesis under ambient conditions: selective electroreduction of dinitrogen to ammonia on black phosphorus nanosheets. *Angew. Chem. Int. Ed.* **58**, 2612–2616 (2019).

33. Xu, G. et al. Nitrogen-doped phosphorene for electrocatalytic ammonia synthesis. *J. Mater. Chem. A* **8**, 15875–15883 (2020).

34. Batmunkh, M. et al. Efficient production of phosphorene nanosheets via shear stress mediated exfoliation for low-temperature perovskite solar cells. *Small Methods* **3**, 1800521 (2019).

35. Favron, A. et al. Photooxidation and quantum confinement effects in exfoliated black phosphorus. *Nat. Mater.* **14**, 826–832 (2015).

36. Lu, W. et al. Plasma-assisted fabrication of monolayer phosphorene and its Raman characterization. *Nano Res.* **7**, 853–859 (2014).

37. Wang, X. et al. Highly anisotropic and robust excitons in monolayer black phosphorus. *Nat. Nanotechnol.* **10**, 517–521 (2015).

38. Yang, S. et al. A delamination strategy for thinly layered defect-free high-mobility black phosphorus flakes. *Angew. Chem. Int. Ed.* **57**, 4677–4681 (2018).

39. Li, J. et al. Ultrafast electrochemical expansion of black phosphorus toward high-yield synthesis of few-layer phosphorene. *Chem. Mater.* **30**, 2742–2749 (2018).

40. Park, B.-W. et al. Stabilization of formamidinium lead triiodide α-phase with isopropylammonium chloride for perovskite solar cells. *Nat. Energy* **6**, 419–428 (2021).

41. Kim, G. et al. Impact of strain relaxation on performance of α-formamidinium lead iodide perovskite solar cells. *Science* **370**, 108–112 (2020).

42. Min, H. et al. Efficient, stable solar cells by using inherent bandgap of α-phase formamidinium lead iodide. *Science* **366**, 749–753 (2019).

43. Liang, Y. et al. Toward stabilization of formamidinium lead iodide perovskites by defect control and composition engineering. *Nat. Commun.* **15**, 1707 (2024).

44. Chen, X. et al. In situ formation of δ-FAPbI3 at the Perovskite/Carbon interface for enhanced photovoltage of printable mesoscopic perovskite solar cells. *Chem. Mater.* **34**, 728–735 (2022).

45. Yang, Y. et al. Interface engineering to eliminate hysteresis of carbon-based planar heterojunction perovskite solar cells via CuSCN Incorporation. *ACS Appl. Mater. Interfaces* **11**, 28431–28441 (2019).

46. Zhang, M. et al. Synergistic cascade carrier extraction via dual interfacial positioning of ambipolar black phosphorene for high-efficiency perovskite solar cells. *Adv. Mater.* **32**, 2000999 (2020).

47. Yu, Y., Hoang, M. T., Yang, Y. & Wang, H. Critical assessment of carbon pastes for carbon electrode-based perovskite solar cells. *Carbon* **205**, 270–293 (2023).

48. Bati, A. S. R. et al. Atomically doped 2D black phosphorus for efficient and stable perovskite solar cells. *Small Struct.* **5**, 2300334 (2024).

49. Calado, P. et al. Evidence for ion migration in hybrid perovskite solar cells with minimal hysteresis. *Nat. Commun.* **7**, 13831 (2016).

50. Tumen-Ulzii, G. et al. Hysteresis-less and stable perovskite solar cells with a self-assembled monolayer. *Commun. Mater.* **1**, 31 (2020).

51. Christians, J. A., Manser, J. S. & Kamat, P. V. Best practices in perovskite solar cell efficiency measurements. avoiding the error of making bad cells look good. *J. Phys. Chem. Lett.* **6**, 852–857 (2015).

52. Wang, Y. et al. Reliable measurement of perovskite solar cells. *Adv. Mater.* **31**, 1803231 (2019).

53. Khenkin, M. V. et al. Consensus statement for stability assessment and reporting for perovskite photovoltaics based on ISOS procedures. *Nat. Energy* **5**, 35–49 (2020).

54. Lee, K. et al. A highly stable and efficient carbon electrode-based perovskite solar cell achieved via interfacial growth of 2D PEA2PbI4 perovskite. *J. Mater. Chem. A* **6**, 24560–24568 (2018).

55. Kobayashi, E., Tsuji, R., Martineau, D., Hinsch, A. & Ito, S. Light-induced performance increase of carbon-based perovskite solar module for 20-year stability. *Cell Rep. Phys. Sci.* **2**, 100648 (2021).

56. Huang, Y. et al. Interaction of black phosphorus with oxygen and water. *Chem. Mater.* **28**, 8330–8339 (2016).

57. Tawfik, S. A., Gould, T., Stampfl, C. & Ford, M. J. Evaluation of van der Waals density functionals for layered materials. *Phys. Rev. Mater.* **2**, 034005 (2018).

58. Pan, Y. et al. Monolayer Phosphorene–metal contacts. *Chem. Mater.* **28**, 2100–2109 (2016).

59. Sun, X., Li, X., Zeng, Y. & Meng, L. Improving the stability of perovskite by covering graphene on FAPbI3 surface. *Int. J. Energy Res* **45**, 10808–10820 (2021).

60. Motta, C. et al. Revealing the role of organic cations in hybrid halide perovskite CH3NH3PbI3. *Nat. Commun.* **6**, 7026 (2015).

61. Egger, D. A. & Kronik, L. Role of dispersive interactions in determining structural properties of organic–inorganic halide perovskites: insights from first-principles calculations. *J. Phys. Chem. Lett.* **5**, 2728–2733 (2014).

62. Cai, Y., Zhang, G. & Zhang, Y.-W. Layer-dependent band alignment and work function of few-layer phosphorene. *Sci. Rep.* **4**, 6677 (2014).

63. Shulenburger, L., Baczewski, A. D., Zhu, Z., Guan, J. & Tománek, D. The nature of the interlayer interaction in bulk and few-layer Phosphorus. *Nano Lett.* **15**, 8170–8175 (2015).

64. Li, R. et al. Strong metal–support interaction for 2D materials: Application in noble metal/TiB2 Heterointerfaces and their enhanced catalytic performance for formic acid dehydrogenation. *Adv. Mater.* **33**, 2101536 (2021).

65. Liu, G. et al. Selective and stable CO_2 electroreduction to CH4 via electronic metal–support interaction upon decomposition/redeposition of MOF. *Small* **19**, 2301379 (2023).

66. Quarti, C., De Angelis, F. & Beljonne, D. Influence of surface termination on the energy level alignment at the $CH_3NH_3PbI_3$ Perovskite/C60 Interface. *Chem. Mater.* **29**, 958–968 (2017).

67. Trinh, Q. T., Bhola, K., Amaniampong, P. N., Jérôme, F. & Mushrif, S. H. Synergistic application of XPS and DFT to investigate metal oxide surface catalysis. *J. Phys. Chem. C* **122**, 22397–22406 (2018).

68. Trinh, Q. T., Tan, K. F., Borgna, A. & Saeys, M. Evaluating the structure of catalysts using core-level binding energies calculated from first principles. *J. Phys. Chem. C* **117**, 1684–1691 (2013).

69. Trinh, Q. T., Yang, J., Lee, J. Y. & Saeys, M. Computational and experimental study of the Volcano behavior of the oxygen reduction activity of PdM@PdPt/C (M=Pt, Ni, Co, Fe, and Cr) core–shell electrocatalysts. *J. Catal.* **291**, 26–35 (2012).

70. Lowe, S. E. et al. Scalable production of graphene oxide using a 3D-printed packed-bed electrochemical reactor with a Boron-doped diamond electrode. *ACS Appl. Nano Mater.* **2**, 867–878 (2019).

71. Blöchl, P. E. Projector augmented-wave method. *Phys. Rev. B* **50**, 17953–17979 (1994).

72. Kresse, G. & Hafner, J. Ab initio molecular dynamics for liquid metals. *Phys. Rev. B* **47**, 558–561 (1993).

73. Kresse, G. & Furthmüller, J. Efficiency of ab-initio total energy calculations for metals and semiconductors using a plane-wave basis set. *Comput. Mater. Sci.* **6**, 15–50 (1996).

74. Klimeš, J., Bowler, D. R. & Michaelides, A. Van der Waals density functionals applied to solids. *Phys. Rev. B* **83**, 195131 (2011).

75. Klimeš, J., Bowler, D. R. & Michaelides, A. Chemical accuracy for the van der Waals density functional. *J. Condens Matter Phys.* **22**, 022201 (2010).

76. Shukla, V., Kumawat, R. L., Jena, N. K., Pathak, B. & Ahuja, R. Electronic and transport properties of bilayer phosphorene nanojunction: effect of paired substitution doping. *ACS Appl Electron Mater.* **3**, 733–742 (2021).

77. Brown, A. & Rundqvist, S. Refinement of the crystal structure of black phosphorus. *Acta Crystallogr.* **19**, 684–685 (1965).

78. Cartz, L., Srinivasa, S. R., Riedner, R. J., Jorgensen, J. D. & Worlton, T. G. Effect of pressure on bonding in black phosphorus. *J. Chem. Phys.* **71**, 1718–1721 (2008).

79. Weller, M. T., Weber, O. J., Frost, J. M. & Walsh, A. Cubic Perovskite structure of black Formamidinium Lead Iodide, α-[HC(NH2)2]PbI3, at 298. *K. J. Phys. Chem. Lett.* **6**, 3209–3212 (2015).

80. Pang, S. et al. $NH_2CH=NH_2PbI_3$: An alternative Organolead Iodide Perovskite sensitizer for mesoscopic solar cells. *Chem. Mater.* **26**, 1485–1491 (2014).

81. Guo, Y. et al. Effects of Rb incorporation and water degradation on the stability of the Cubic Formamidinium Lead Iodide Perovskite surface: a first-principles study. *J. Phys. Chem. C* **121**, 12711–12717 (2017).

82. Tang, W., Sanville, E. & Henkelman, G. A grid-based Bader analysis algorithm without lattice bias. *J. Condens. Matter Phys.* **21**, 084204 (2009).

83. Henkelman, G., Arnaldsson, A. & Jónsson, H. A fast and robust algorithm for Bader decomposition of charge density. *Comput. Mater. Sci.* **36**, 354–360 (2006).

Acknowledgements

Author contributions

P.M. prepared the eBP samples and fabricated PV devices. S.S. and M.B-E. carried out UV-vis spectroscopy, XPS and UPS measurements. Q.T.T., T.G., and N.T.N. carried out DFT calculations and data interpretation. E.C. helped to design and fabricate PBER system for sample preparations. M.T.H., W.H.C., Q.L. and H.W. conducted EQE, PL and water contact angle measurements. Y.L.Z. and M.B. supervised and designed the project. P.M. and M.B. conceived the idea. P.M. carried out all other measurements, data analysis and wrote the first draft. All authors contributed to writing the final version of the manuscript.

Competing interests

The authors declare no competing interests.

Additional information

Supplementary information The online version contains supplementary material available at https://doi.org/10.1038/s41699-024-00476-7.

Correspondence and requests for materials should be addressed to Yu Lin Zhong or Munkhbayar Batmunkh.

Reprints and permissions information is available at http://www.nature.com/reprints

Publisher's note Springer Nature remains neutral with regard to jurisdictional claims in published maps and institutional affiliations.